Three-Dimensional Coupled Finite-Element Analyses of the Seismic Performance of Onshore Wind Turbines on Liquefiable Soils

Domenico Gaudio, Ph.D.[1]; Juntae Seong[2]; Stuart Haigh, Ph.D.[3]; Giulia M. B. Viggiani, Ph.D.[4]; Gopal S. P. Madabhushi, Ph.D.[5]; Rajesh Shrivatsava[6]; Ravikant Veluvolu[7]; and Prashanta Padhy[8]

Abstract: In recent decades, research on renewable energy has been boosted by the emerging awareness of energy security and climate change and their consequences, such as the global cost of adapting to the climate impacts. Both onshore and offshore wind turbine farms have been considered as one of the main alternatives to fossil fuels. Their development currently involves seismic-prone areas, such as the Californian coastline and East Asia, where the risk of soil liquefaction is significant. Onshore wind turbines (OWTs) typically are founded on shallow rafts. Their operation can be affected strongly by the simultaneous presence of intense earthquakes and wind thrust, which may cause remarkable permanent tilting and loss of serviceability. In these conditions, accurate evaluation of the seismic performance of these structures requires the development of well-validated numerical tools capable of capturing the cyclic soil behavior and the build-up and contextual dissipation of seismic-induced pore-water pressures. In this paper, a numerical model developed in OpenSees, calibrated against the results of dynamic centrifuge tests, was used to evaluate the influence of some ground motion intensity Measures of the seismic behavior of OWTs included the amplitude, frequency content, strong-motion duration, and Arias intensity (energy content) of the earthquake, together with the effect of a coseismal wind thrust, which is not well explored in the literature. The seismic performance of an OWT was assessed in terms of peak and permanent settlement and tilting, the latter of which was compared with the threshold of 0.5° typically adopted in practice.
DOI: 10.1061/JGGEFK.GTENG-11807.

Author keywords: Onshore wind turbine (OWT); Liquefaction; Three-dimensional (3D) finite-element analyses; *u-p* formulation; OpenSees; Numerical modeling; Centrifuge testing; Earthquakes.

Introduction

Onshore and offshore wind have established themselves as a reliable and sustainable form of renewable energy. In developing countries such as India and other Southeast Asian countries, onshore wind can be very attractive and cheaper than offshore wind, especially when the wind farms can be located in otherwise unusable lands such as salt marshes. However, in many areas of these countries there is a significant risk of soil liquefaction. For example, during the Bhuj earthquake of 1999 in India, extensive liquefaction occurred in the Kutch region (Madabhushi et al. 2005). The performance of the foundations of onshore wind farms needs to be established, especially in terms of their settlements and rotations, because there are strict serviceability limits requiring, e.g., that the rotation of the foundation at ground level must be less than 0.5° (DNV 2010). Moreover, it is likely that each wind farm will have hundreds of individual wind turbines, and the foundations for these may be similar from an economy-of-scale point of view. Typically, raft foundations are used for onshore wind turbines. Well-validated numerical tools are required to evaluate the seismic performance of individual rafts at selected locations of the wind farm in order to establish the satisfactory performance of the wind turbine–foundations system under seismic loading, especially when the foundation soil is liable to liquefaction (Vacareanu et al. 2019).

Early research on raft foundations of onshore wind turbines on liquefiable soils was carried out using dynamic centrifuge testing by Seong et al. (2022) for selected soil profiles and for a combination of scaled real earthquake motions and strong sinusoidal motions. The results of these tests indicated that, for the specific case at hand, the raft foundations could settle and rotate significantly without ground improvement. Although the residual rotations were within the limit of 0.5°, the dynamic rotations exceeded this limit during some of the strong motions, and the overall settlement was more than 0.8 m.

[1]Assistant Professor, Dept. of Engineering, Univ. of Cambridge, Cambridge CB3 0EF, UK; Assistant Professor, Dipartimento di Ingegneria Strutturale e Geotecnica, Sapienza Università di Roma, Rome 00184, Italy (corresponding author). ORCID: https://orcid.org/0000-0001-8957-5764. Email: domenico.gaudio@uniroma1.it

[2]Ph.D. Candidate, Dept. of Engineering, Univ. of Cambridge, Cambridge CB3 0EF, UK. ORCID: https://orcid.org/0000-0003-3782-0099

[3]Professor, Dept. of Engineering, Univ. of Cambridge, Cambridge CB3 0EF, UK.

[4]Professor, Dept. of Engineering, Univ. of Cambridge, Cambridge CB3 0EF, UK. ORCID: https://orcid.org/0000-0002-0993-0322

[5]Professor, Dept. of Engineering, Univ. of Cambridge, Cambridge CB3 0EF, UK.

[6]Chief Operating Officer, Adani Green Energy Limited, Shantigram, Near Vaishnodevi Circle, S G Highway, Ahmedabad, Gujarat 382421, India.

[7]Vice President (Technology), Adani Green Energy Limited, Shantigram, Near Vaishnodevi Circle, S G Highway, Ahmedabad, Gujarat 382421, India.

[8]Deputy General Manager, Adani Green Energy Limited, Shantigram, Near Vaishnodevi Circle, S G Highway, Ahmedabad, Gujarat 382421, India.

Note. This manuscript was submitted on March 28, 2023; approved on December 26, 2023; published online on February 29, 2024. Discussion period open until July 29, 2024; separate discussions must be submitted for individual papers. This paper is part of the ***Journal of Geotechnical and Geoenvironmental Engineering***, © ASCE, ISSN 1090-0241.

In this paper, a numerical model with u-p formulation, developed in OpenSees and calibrated against the results of dynamic centrifuge tests, is used to explore the effects of the characteristics of the ground motion on the seismic behavior of onshore wind turbines (OWTs). Moreover, the paper addresses the impact of the presence of a coseismal wind thrust, which still is not well explored in the literature.

An advanced constitutive model known as Sanisand (Dafalias and Manzari 2004) already is available in the library of OpenSees, so the excess pore-pressure generation under cyclic loading in saturated soils could be captured accurately, although some limitations have been detected in the literature, namely a typical overprediction of the rate of pore-pressure dissipation and some excessive dilative tendency, which usually leads to excessively large acceleration spikes (Ramirez et al. 2018). The Sanisand constitutive parameters of the sand adopted in the dynamic centrifuge tests were determined originally by Salvatore et al. (2017) based on the results of triaxial tests. These constitutive parameters, and particularly those relevant to cyclic loading, subsequently were modified slightly by Gaudio et al. (2023) to reproduce numerically the generation of excess pore water pressures observed in the centrifuge tests by Seong et al. (2022). Ad hoc calibration for boundary value problems was suggested by Ramirez et al. (2018), who pointed out that the usual calibration based only on element tests typically does not yield good predictions for seismic site performance in a centrifuge.

The same modified constitutive parameters were used for all the analyses presented in this paper. After extensive validation of the numerical model against the results of dynamic centrifuge tests, which mainly was performed by Gaudio et al. (2023) and is summarized in the present paper, a numerical study was carried out to investigate the effects of different intensity measures (IMs) of the applied acceleration time histories on the dynamic performance of the wind turbine–raft system. The IMs considered in the study include measures of amplitude and frequency content, strong motion duration, and Arias intensity. Further numerical analyses were carried out to investigate the effect of the simultaneous application of operational wind load at the serviceability limit state (SLS) and the seismic loading on the dynamic and residual rotation of the raft foundation, as recommended by DNV (2021). These standards are applicable to all types of onshore and fixed offshore support structures for wind turbines (DNV 2018).

Problem Definition

Fig. 1 shows the layout of the problem considered in the parametric study. The tower of the onshore wind turbine has height $h_s = 48$ m, total mass $m_{\text{tot}} = 435.8$ Mg (t) and a fixed-base natural frequency $f_s \approx 0.3$ Hz; its lumped mass is equal to 153.6 Mg, which mimics that of the rotor–nacelle assembly (RNA). The dimensions of the wind turbine were selected to satisfy two conditions: (1) the tower had to fit the centrifuge facility without hitting the ceiling; and (2) the fixed-base OWT frequency had to be in the range 0.20–0.30 Hz to be representative of a 5-MW OWT (Desmond et al. 2016), although scaled down for the space constraints imposed by the centrifuge. The circular raft foundation (diameter $D = 15.4$ m, and thickness $s = 1.6$ m) rested on a fully saturated loose sand layer with a relative density $D_R = 43\%$ and a thickness of 15 m, which was underlain by a dense sand layer with $D_R = 90\%$ and thickness of 12 m. The bearing pressure exerted by the structure on the sand layer was $q = 58.8$ kPa. The shallow layer was composed of a partially excavated clay ($H_1 = 3.2$ m), which was replaced with gravel in the vicinity of the tower. These values were selected to represent a typical configuration for an OWT on liquefiable soils, following Gaudio et al. (2023). Base excitations were applied at the base of the model ($y = -30.2$ m) in the horizontal x-direction in terms of horizontal acceleration time history, therefore assuming a rigid bedrock.

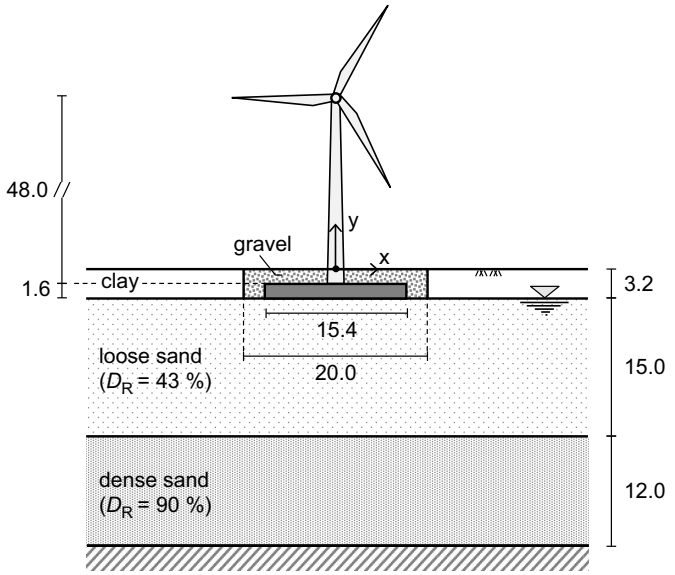

Fig. 1. Layout of the problem with dimensions in meters. (Adapted from Gaudio et al. 2023.)

Experimental Setup for Dynamic Centrifuge Tests

A reduced-scale model of the problem layout presented in the previous section was prepared and tested in the Turner beam centrifuge at Schofield Centre, University of Cambridge, UK. The model was contained in an equivalent shear beam (ESB) box and was spun at a nominal centrifugal acceleration of 80 g. The experimental setup hereby described was part of a centrifuge campaign aimed at evaluating the performance of different mitigation techniques for OWTs on shallow foundations resting on liquefiable soils, such as stone columns (Seong et al. 2022), connected piles, and disconnected piles. The effect of these techniques was evaluated in terms of

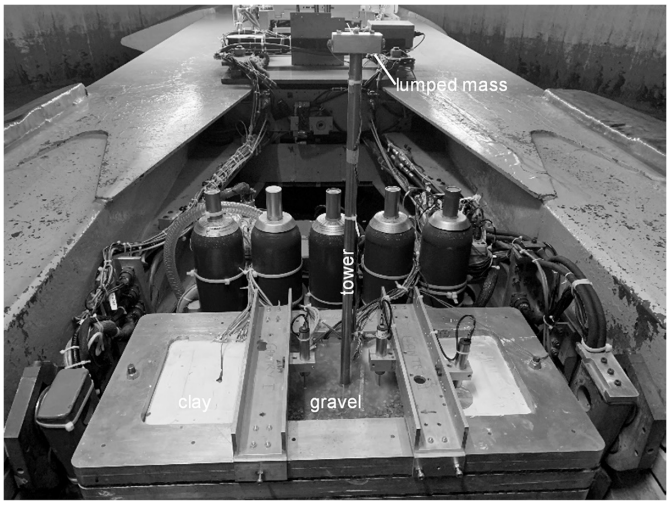

Fig. 2. Model loaded on the centrifuge.

Table 1. Physical properties of Hostun HN31 sand

Property	Value
G_s	2.65
e_{max}	1.011
e_{min}	0.555
φ'_{cv} (degrees)	33

Source: Data from Adamidis and Madabhushi (2022).

seismic performance indices which are adopted in typical practice, such as the dynamic and permanent settlement and tilting of the OWT.

Fig. 2 shows the model as loaded in the centrifuge. The clayey and gravelly soils are visible, along with the tower and the lumped mass representing the OWT considered in this study. In the model, the tower was modeled using a steel hollow tube with an outer diameter $D_{out} = 17.5$ mm (1.4 m at the prototype scale) and a wall thickness $s_w = 2.5$ mm (0.2 m), which therefore was characterized by a bending stiffness $EI \approx 0.72$ kN · m^2 (29.29 GN · m^2). The head mass was reproduced using a brass lumped mass $m_{lump} = 300$ g (153.6 Mg), and the raft foundation (not visible in Fig. 2) was modeled using a circular aluminum plate with a diameter of 192 mm (15.36 m at prototype scale) and a thickness of 20 mm (1.6 m).

Both the loose and the dense sand consisted of Hostun HN31 sand, the physical properties of which are given in Table 1. The target values of relative densities adopted in this paper, namely $D_R = 43$ and 90%, first were achieved via air pluviation (Madabhushi et al. 2006); the sand layers then were fully saturated by adopting a fluid with a viscosity of 80 MPa · s, following Adamidis and Madabhushi (2015).

The model tested in the centrifuge was instrumented with miniature piezoelectric accelerometers, microelectrical mechanical systems (MEMS), pore-pressure transducers (PPTs), and LVDTs (Fig. 3). An air hammer device (AHD) was used to generate shear waves in the model and measure their propagation velocity.

The model was subjected to a series of base excitations (BEs) imposed at the base of the ESB box using the servohydraulic shaker described by Madabhushi et al. (2012). Three different ground motions were applied in the test, namely the recorded accelerations for the Imperial Valley and Kobe earthquakes and a train of sine waves; further details of the centrifuge model were given by Seong et al. (2022). Fig. 4 shows the dimensionless acceleration time histories and the Fourier amplitude spectra of the signals which were applied at the bottom of the numerical model, together with the acceleration response spectra computed for a damping ratio $\xi = 5\%$. These base excitations differed from those adopted in the centrifuge for the eighth-order Butterworth filter type characterized by a low-pass frequency $f_{max} = 4$ Hz.

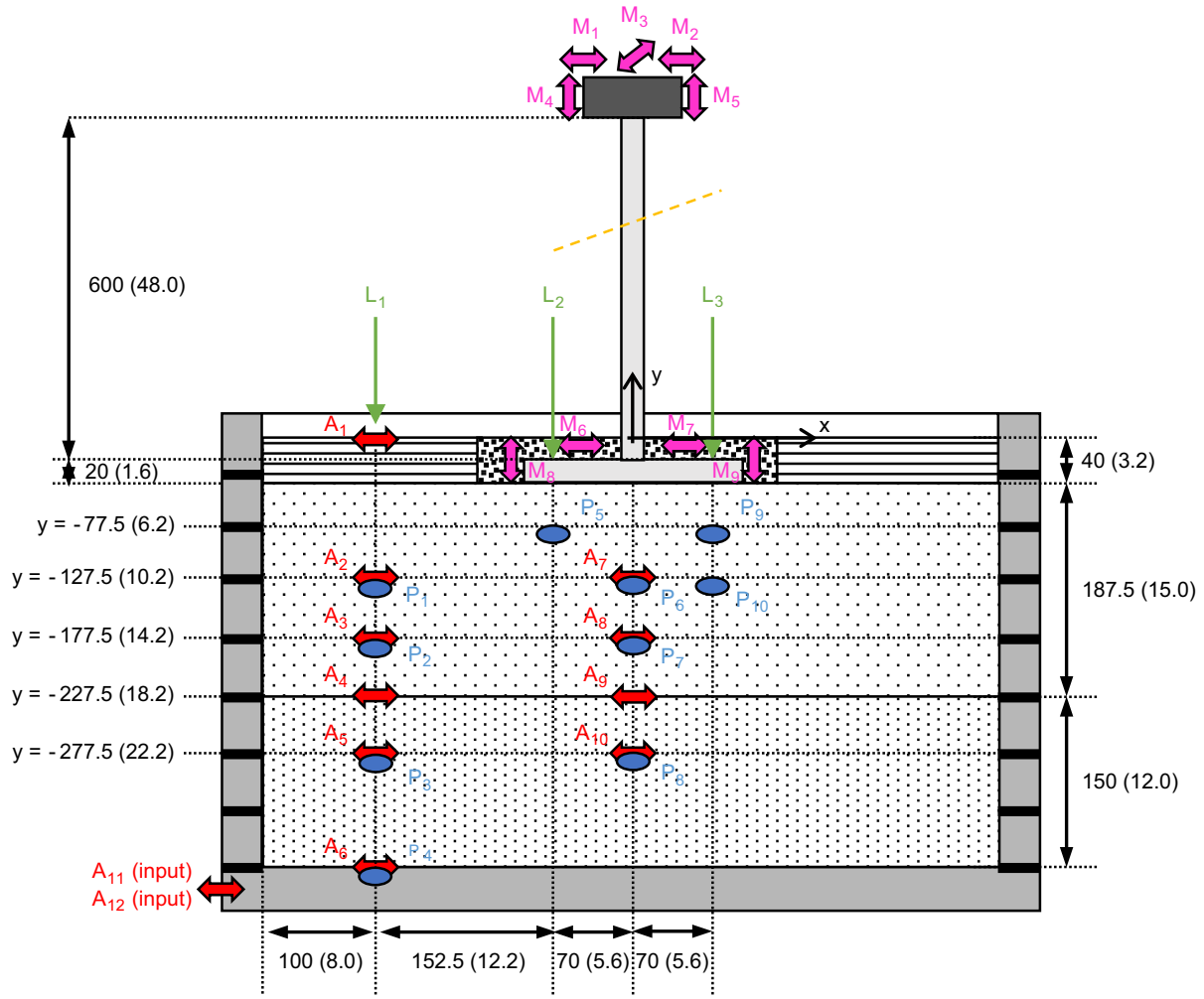

Fig. 3. Layout of the instrumentation adopted in the centrifuge test at model scale (mm). Values in parentheses are prototype dimensions (m). (Adapted from Gaudio et al. 2023.)

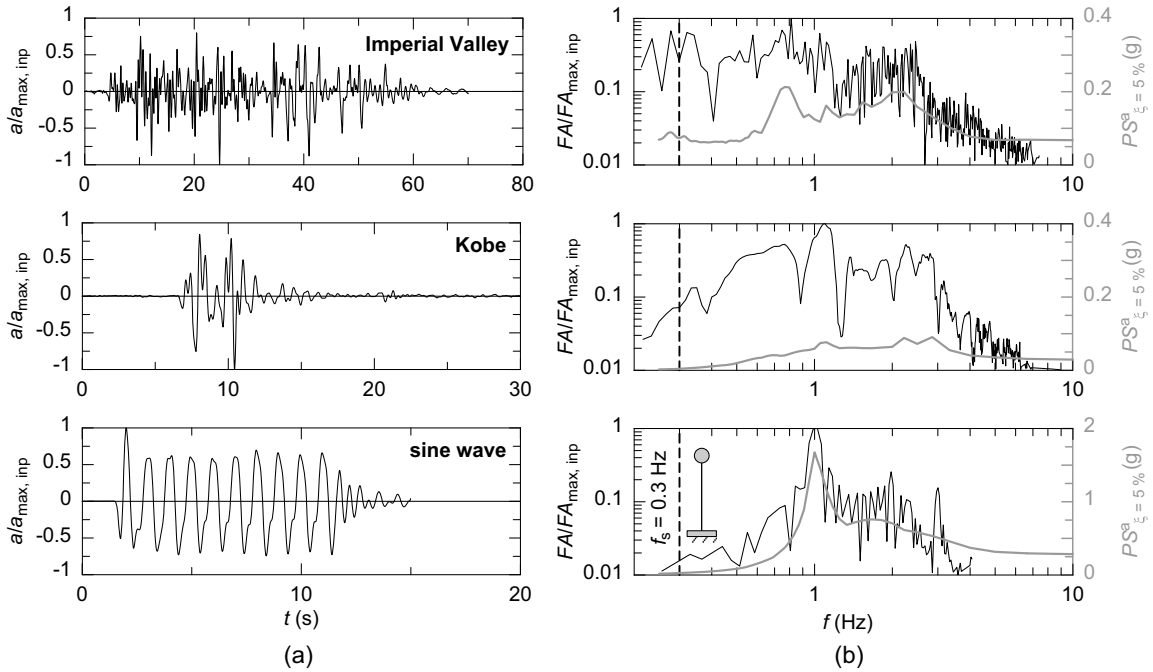

Fig. 4. Input ground motions: (a) dimensionless acceleration time histories; and (b) dimensionless Fourier amplitude and dimensional acceleration response spectra.

The Fourier amplitude spectra in Fig. 4 have been smoothened using a centered moving average with an interval of 10. In Fig. 4(b), the fixed-base frequency of the OWT is indicated as a dashed line.

Three-Dimensional Nonlinear Dynamic Finite-Element Analyses

A three-dimensional (3D) finite-element (FE) model reproducing the ESB container at prototype scale was implemented in OpenSees MP v.3.3.0 (Tarque Ruiz 2020) for four-processor parallel computing. The numerical model included relatively close boundaries representing the walls of the ESB container adopted in the experimental work, and its accuracy was tested by directly comparing the experimental results with those of the numerical simulations. The effects of the relatively close boundaries on the dynamic response of the system were assessed by Gaudio et al. (2023), in which the numerical results obtained using a small model, reproducing the physical dimensions of the ESB box were compared with those resulting from a large model in which boundaries were placed at a sufficient distance from the structure so as not to play any role, according to Gaudio and Rampello (2016) (Fig. 5). These effects were found to be marginal, confirming, for an extended set of input acceleration time histories, that the behavior of the system can be reproduced in less computationally expensive analyses carried out on a smaller numerical domain without any significant loss of accuracy. Incidentally, the results of the analyses also gave confidence in the validity of the dynamic centrifuge tests carried out in the ESB model container (Seong et al. 2022).

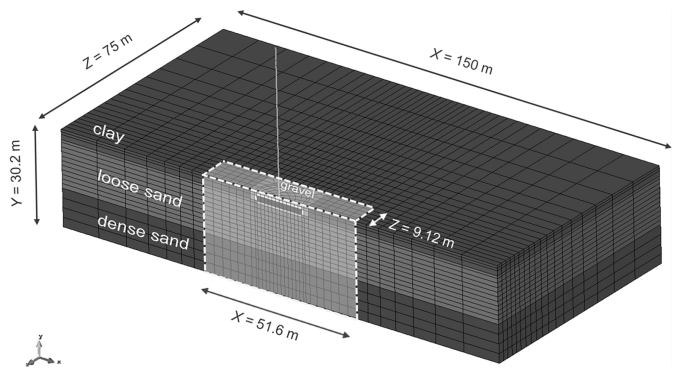

Fig. 5. Large and small (shaded volume) 3D FE models.

The small numerical model was used in this work to assess the relative influence of ground motions and wind thrust, as discussed in the following. All dimensions reported herein are at prototype scale, unless specified otherwise.

Table 2 summarizes the characteristics of the seismic signals adopted in the numerical analyses, where $a_{max,inp}$ is the peak acceleration, $f_{p,inp}$ is the predominant frequency, i.e., the peak amplitude of the Fourier spectrum (Kramer 1996), $D_{5–95,inp}$ is the strong-motion duration as defined by Trifunac and Brady (1975), and $I_{A,inp}$ is the Arias intensity (Arias 1970). The adopted signals span a broad range of values of IMs, namely $a_{max,inp} = 0.03–0.40$ g, $f_{p,inp} = 0.50–2.00$ Hz, $D_{5-95,inp} = 3.97–40.82$ s, and $I_{A,inp} = 0.01–7.51$ m/s. The real acceleration time histories recorded during the earthquake of Imperial Valley and Kobe were scaled both up and down by a constant amplification factor F, which was applied to the entire time trace; hence, both their $a_{max,inp}$ and $I_{A,inp}$ values were affected by this procedure. In Table 2, the base excitations are grouped in terms of Arias intensity in five categories: very weak, weak, moderate, strong, and very strong. Some of the base excitations correspond to those imposed in the centrifuge testing campaign, as detailed subsequently.

The shaded volume in Fig. 5 represents the FE numerical model considered in the study considered in the study, which is compared with the large model mentioned above. Taking advantage of the symmetry of the problem, this small 3D model reproduced only one-half of the ESB box, and had dimensions $X = 51.6$ m ($\approx 3.4D$), $Z = 9.12$ m ($\approx 0.6D$) and $Y = 30.2$ m ($\approx 2D$). The mesh consisted of 3,121 nodes and 2,401 elements, with a progressively

Table 2. Base excitations applied in numerical analyses

Base excitation	Ground motion	Intensity	$a_{max,inp}$ (g)	$f_{p,inp}$ (Hz)	$D_{5–95,inp}$ (s)	$I_{A,inp}$ (m/s)
BE_1	1995 Kobe (Port Island N-S)	Very weak	0.03	1.10	3.97	0.01
BE_2	1979 Imperial Valley (Cerro Prieto N-S)	Weak	0.07	0.81	40.82	0.21
BE_3	Sine wave		0.10	2.00	9.44	0.26
BE_4			0.10	1.00	9.40	0.27
BE_5			0.10	0.50	9.78	0.30
BE_6		Moderate	0.19	2.00	9.44	0.96
BE_7			0.19	1.00	9.40	1.00
BE_8			0.19	0.50	9.78	1.09
BE_9	1995 Kobe (Port Island N-S)		0.40	1.10	3.97	1.68
BE_10	Sine wave	Strong	0.32	2.00	9.44	2.68
BE_11			0.28	1.00	9.37	2.74
BE_12			0.32	1.00	9.40	2.80
BE_13			0.32	0.50	9.78	3.04
BE_14		Very strong	0.40	2.00	9.44	4.18
BE_15			0.40	1.00	9.40	4.36
BE_16	1979 Imperial Valley (Cerro Prieto N-S)		0.40	0.81	40.82	7.51

finer mesh approaching the raft foundation. BrickUP elements were assigned to the whole domain; these are hexahedral linear isoparametric FEs characterized by eight nodes with four degrees of freedom each—three for solid displacements, and one for fluid pressure—and by eight Gauss points per element. The mode of the maximum size of these finite elements was equal to 3.3 m, and the maximum size was selected to fulfil the requirement provided by Kuhlemeyer and Lysmer (1973), thus avoiding numerical distortion of waves propagating into the model. To this end, the vertical distance between two adjacent nodes, Δy, was checked to satisfy, at every depth, the following condition:

$$\Delta y \leq \frac{\lambda_{min}}{6} = \frac{V_S}{6 \cdot f_{max}} \quad (1)$$

where λ_{min} = minimum wavelength expected to travel into the FE model; V_S = soil shear wave velocity; and f_{max} = maximum frequency travelling into the FE model (4 Hz). Mobilized values of the shear wave velocity V_S were considered at every depth in Eq. (1), where the term "mobilized" indicates values that are consistent with the shear strain level induced by the seismic shaking. The strain level was computed by preliminary performing a one-dimensional (1D) ground response analysis with the linear equivalent method (LEM) (Idriss and Seed 1968), in which the initial (small-strain) shear wave velocity profile was evaluated at every depth referring to the experimental and empirical profiles reported by Gaudio et al. (2023).

The tower was modeled using Timoshenko beam elements to consider the shear deformability of the tower, although this was recognized as of minor importance in the global response of the pier; a top lumped mass representing the brass mass modeled in the centrifuge was simulated.

Table 3. Values of PIMY parameters assumed for clay layer

Parameter	Value
ρ (Mg/m^3)	1.3
G^{ref} (MPa)	13
K^{ref} (MPa)	65
c (kPa)	18
γ_{max}	0.1
φ (degrees)	0
d	0

In the initial static (gravity) calculation phase, standard boundary conditions were applied to the model, i.e., $u_x = 0$ along the lateral y-z boundaries, $u_z = 0$ along the x-y boundaries, and fixed nodes at the base of the mesh ($u_x = u_y = u_z = 0$). When switching to the dynamic calculation phase, the restraints on the horizontal displacements at the base of the mesh were removed and periodic constraints were applied to the nodes along the vertical x-z boundaries, which implies that the nodes on the domain edges are tied together so as not to have any relative horizontal displacement ($\Delta u_x = 0$). This may be considered equivalent to the free-field pure-shear conditions applied by the end walls of the ESB container. Hydraulic boundary conditions were set up with the water table located at the top of the loose sand: pore-water pressures were allowed to fluctuate freely for all nodes within the sand layers ($y \leq -3.2$ m), whereas both steady and excess pore-water pressures were inhibited in the clay and gravel layers along with the raft foundation ($p = \Delta p = 0$).

The pressure-independent multiyield (PIMY) and the pressure-dependent multiyield (PDMY) models were adopted to describe the mechanical behavior of the clay and the gravel, respectively, whereas Sanisand04 was adopted for all sand layers. Typical values provided by Yang et al. (2008) for soft clay and medium dense sand were adopted to mimic the cyclic response of the clay and the gravel, respectively (Tables 3 and 4). Table 5 summarizes the

Table 4. Values of PDMY parameters assumed for gravel layer

Parameter	Value
ρ (Mg/m^3)	2
G^{ref} (MPa)	100
K^{ref} (MPa)	300
φ (degrees)	37
φ_{PT} (degrees)	27
γ_{max}	0.1
d	0.5
c	0.05
d_1	0.6
d_2	3
I_1 (kPa)	5
I_2	0.003
I_3	1
n	20
e	0.55

Table 5. Values of Sanisand parameters and hydraulic conductivity assigned to BrickUP elements

Sand	e_{init}	ρ (Mg/m^3)	G_0	ν	M	c	e_0	λ_c	ξ	m	h_0	c_h	n^b	A_0	n^d	z_{max}	c_z	k (m/s)
Loose	0.813	1.947	293	0.05	1.3	0.712	1.13	0.13	0.45	0.02	1.82	0.968	1.1	0.33	3.5	10	1,000	1.48×10^{-4}
Dense	0.600	2.071	293	0.05	1.3	0.712	1.13	0.13	0.45	0.02	1.82	0.968	1.1	0.33	3.5	10	1,000	6.74×10^{-5}

constitutive parameters adopted for Sanisand04 and the hydraulic conductivity assigned to the BrickUP elements; these were calibrated by Gaudio et al. (2023) using the acceleration and pore-water pressure build-up recorded along the far-field array in the centrifuge tests.

The raft and the tower were assigned isotropic linear viscous-elastic materials with the mechanical parameters representing those of aluminum (mass density $\rho_a = 2.70$ Mg/m^3, Young's modulus $E_a = 70$ GPa, and Poisson's ratio $\nu_a = 0.15$) and steel ($\rho_s = 7.80$ Mg/m^3, $E_s = 210$ GPa, and $\nu_s = 0.30$), respectively.

The contact between raft and the soil was simulated using thin continuum layers with the stiffness moduli and shear strength reduced by factors of 2/3 and 3/4, respectively (Kementzetzidis et al. 2019); this applied to the contacts of the foundation with both the gravel and the loose sand. Hence, the following parameters were adopted: $G^{ref} = 66.67$ MPa, $K^{ref} = 200$ MPa, and $\varphi = 29.5°$ for the gravel–foundation interface; and $G_0 = 195.33$ MPa and $M_c = 0.975$ for the loose sand–foundation interface. This manner of reproducing the raft–soil contact does not permit soil separation or gapping to be simulated. This choice was made because soil gapping was not observed during the centrifuge tests, which may be attributed to both the high superstructure weight and the overburden pressure applied by the gravel layer to the foundation.

A small amount of viscous damping was added in the model using the Rayleigh formulation. Both the soils and the raft were assigned a damping ratio $\xi_{soil} = 1\%$, whereas the value $\xi_{turbine} = 3\%$ was attributed to the tower and its lumped mass. The value attributed to the soils was assigned with the twofold objective of providing some energy dissipation at the very low strains and of attenuating possible spurious, nonphysical high-frequency noise in the model, whereas the value assigned to the tower and its lumped mass was obtained from experimental impact hammer tests performed at $1g$ on the fixed-base tower. The fixed-base damping ratio of the tower could be extrapolated to the full-scale turbine model due to two concurring conditions, namely the linear elastic behavior exhibited by the superstructure during the whole experimental campaign, and the fact that the damping ratio is a dimensionless quantity, and therefore is not affected by the scaling procedure.

The 3D nonlinear dynamic analyses were performed using automatic time stepping (Δt), with a maximum $\Delta t_{max} = 0.0133$ s. This corresponded to the sampling rate used in the centrifuge (6 kHz) at prototype scale. When the soil approached liquefaction, to obtain convergence it was necessary to subdivide the time step 32 times, corresponding to $\Delta t \approx 0.0004$ s. Newmark's time stepping method (Newmark 1959) was used to integrate the equations of motion with values $\beta = 0.60$ and $\gamma = 0.3025$, and the Krylov–Newton solution algorithm (Scott and Fenves 2010) was chosen to handle nonlinear soil behavior.

The outcome of the calibration of the hydromechanical sand parameters performed by Gaudio et al. (2023) is given in Fig. 6,

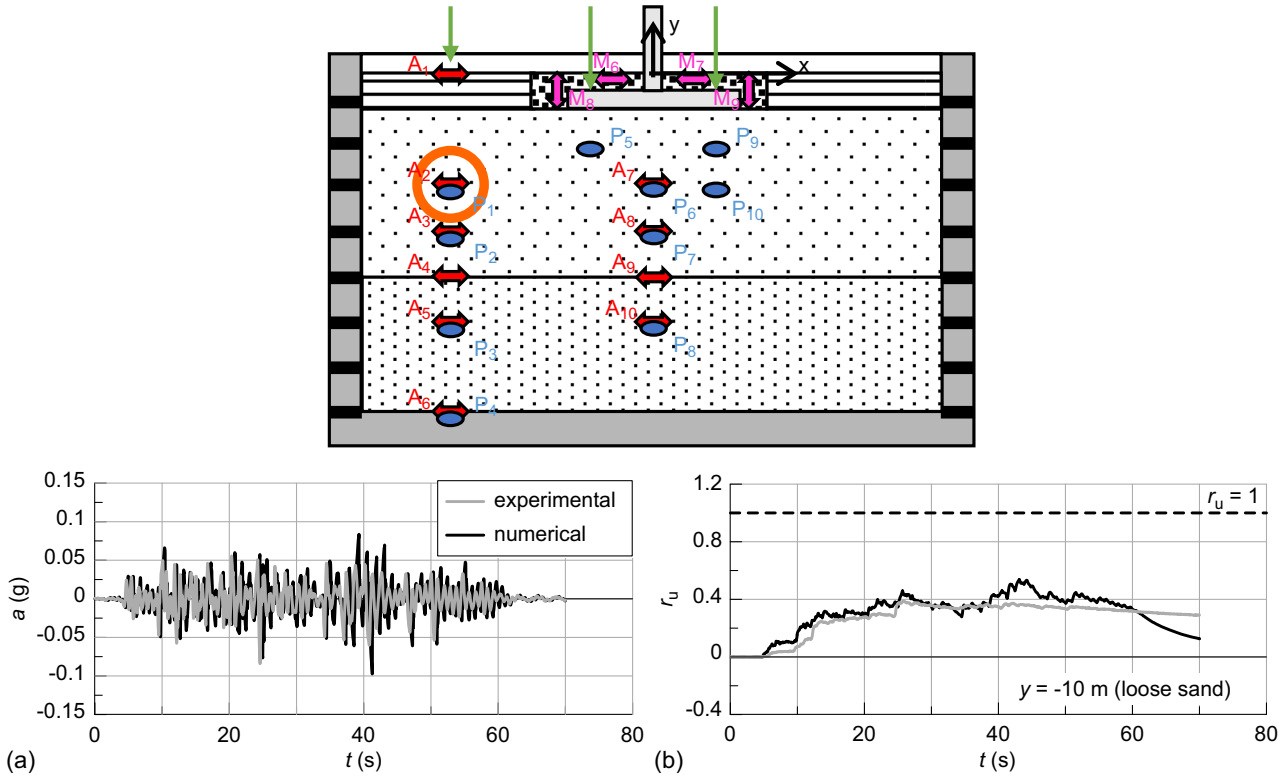

Fig. 6. Experimental and numerical time histories recorded in the loose sand layer obtained with the weak Imperial Valley motion (BE_2): (a) horizontal acceleration; and (b) excess pore-water pressure ratio.

J. Geotech. Geoenviron. Eng., 2024, 150(5): 04024030

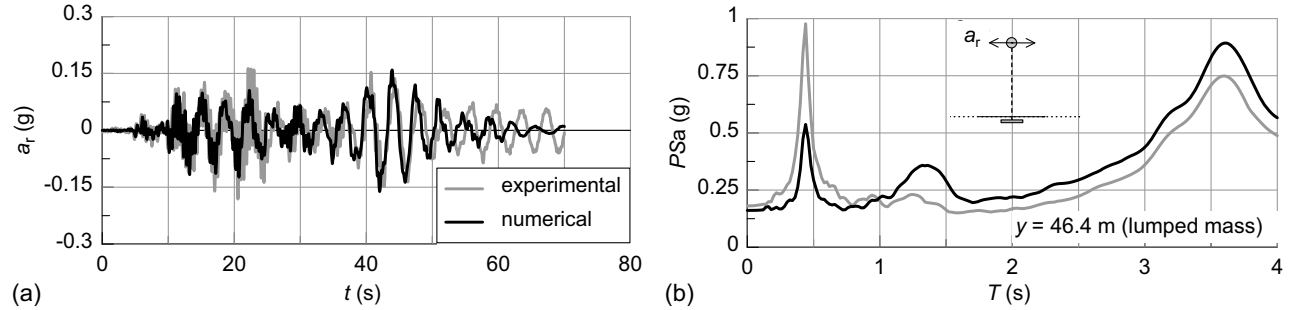

Fig. 7. Experimental and numerical results at the top of the tower: (a) horizontal acceleration time histories; and (b) elastic acceleration spectra for the weak Imperial Valley base excitation (BE_2).

which shows the results obtained in the loose sand layer ($y = -10$ m) for the weak Imperial Valley motion ($a_{\max,\text{inp}} = 0.07g$). This is a blind prediction of the excess pore-water pressures, because parameter calibration had been performed previously using the experimental results obtained for a sinusoidal motion (Gaudio et al. 2023). The results are given in terms of time histories of the horizontal acceleration, a, and excess pore-water pressure ratio

$$r_u = \frac{\Delta p}{\sigma'_{v0}} \tag{2}$$

where σ'_{v0} = effective vertical stress in geostatic conditions; and Δp = excess pore-water pressure. Good agreement between the experimental and the numerical results is apparent, in terms of both peak values $a_{\max}$ and $r_{u,\max}$.

The predicted seismic response of the raft foundation and of the tower (Fig. 7) also compared favorably with the experimental observations, as demonstrated by Gaudio et al. (2023) for a different seismic input. For the raft, not shown here for the sake of brevity, the quantities of interest were the settlement relative to the far-field, w_{rel}, and its rigid rotation, θ

$$\begin{aligned} w_{\text{rel}}(t) &= \bar{w}(t) - w_{ff}(t) \\ \theta(t) &= \frac{[w_1(t) - w_2(t)]}{d_{12}} \end{aligned} \tag{3}$$

where $\bar{w} = [w_1(t) + w_2(t)]/2$ = average settlement of raft; w_1 and w_2 = settlements at left and right sides of the foundation, respectively; $w_{\text{ff}}(t)$ = far-field settlement (recorded by LVDT L_1 in Fig. 3); and $d_{12} = 11.2$ m = distance between the two LVDTs located close to the edges of the raft (L_2 and L_3 in Fig. 3). Table 6 presents the peak relative settlement and rotation obtained from the centrifuge tests and the numerical analyses, for the base excitations applied in the centrifuge. The performance of the numerical model can be deemed satisfactory, even in a large span of seismic intensity, as demonstrated by the good agreement obtained for both BE_1 and BE_15, which are representative of a very weak and a strong motion, respectively. This outcome provided confidence in the numerical model adopted in this study.

The tower response is given in Fig. 7 in terms of acceleration time histories and elastic acceleration spectra at the lumped mass level. The numerical results were in accordance with the experimental results, in terms of both peak values of acceleration [Fig. 7(a)] and frequency content [Fig. 7(b)]. In particular, the first two fundamental periods of the system were well reproduced in the numerical model. The numerical value of spectral acceleration at the first fundamental period of the system ($T = 3.60$ s) was only 20% larger than that observed experimentally, whereas the numerical spectral acceleration at $T = 0.44$ s was significantly smaller (by about −43%) than that observed experimentally. The observed overdamping of the second eigenperiod of the system also may responsible for the lower accelerations obtained from the numerical simulations at the end of the time trace in Fig. 7(a). A possible increase of the structural damping would worsen the numerical prediction at the fundamental period $T = 3.60$ s and adversely affect the value of PSa at $T = 0$, which is well captured using the current value of the damping ratios.

Influence of Ground Motion Characteristics

From the previous section it is apparent that the small FE model may be adopted to be representative of the centrifuge tests. The small FE model was used to investigate the influence of the amplitude, frequency, strong-motion duration, and Arias intensity of the sinusoidal input motion and scaled realistic motions on the dynamic performance of the wind turbine–raft system, as summarized in this section.

Amplitude

The influence of amplitude was assessed to study what would happen if rare and intense ground motions hit the OWT. This was achieved by comparing the results obtained with the scaled Imperial Valley excitations (BE_2 and BE_16), which are characterized by peak accelerations $a_{\max,\text{inp}} = 0.07$ and $0.40g$.

Fig. 8 presents the results obtained along the far-field alignment with the weak (BE_2) and very strong (BE_16) Imperial Valley ground motions for the loose sand layer (depth $y = -10$ m), in

Table 6. Maximum permanent relative settlements and peak rotations from centrifuge tests and numerical analyses

Base excitation	Ground motion	Intensity	$a_{\max,\text{inp}}$ (g)	$w_{\text{relperm,exp}}$ (m)	$w_{\text{relperm,num}}$ (m)	$\theta_{\max,\text{exp}}$ (degrees)	$\theta_{\max,\text{num}}$ (degrees)
BE_1	1995 Kobe (Port Island N-S)	Very weak	0.03	0.01	0.01	0.04	0.01
BE_2	1979 Imperial Valley (Cerro Prieto N-S)	Weak	0.07	0.02	0.13	0.09	0.05
BE_11	Sine wave	Strong	0.28	0.45	0.42	0.20	0.20

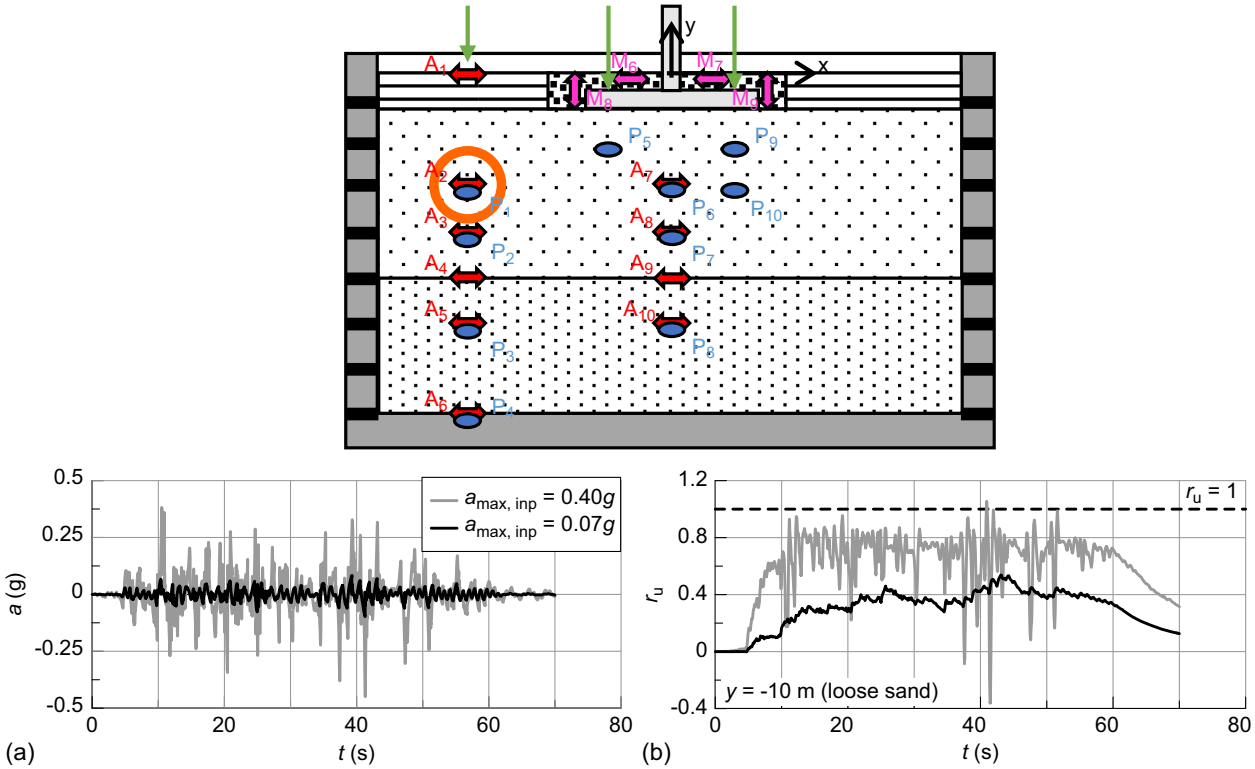

Fig. 8. Far-field response in the loose sand layer for the Imperial Valley base excitations (BE_2 and BE_16).

terms of both time histories of the horizontal acceleration, a, and the excess pore-water pressure ratio, r_u. Higher values of a and r_u were reached when applying the BE_16 ground motions, which were intense enough to trigger full liquefaction at some time instant ($r_u = 1$), compared with $r_{u,\max} = 0.5$ reached for the weak motion. Although this was somewhat expected, it is interesting that spurious high-frequency, sharp acceleration spikes arose in the horizontal acceleration time histories which were beyond the peak value of the input ($a = 0.45g > a_{\max,\text{inp}}$). This is attributable mainly to the recovery of soil shear strength due to the instantaneous decrease of the excess pore-water pressure ratio, r_u, because it is quite apparent at time $t = 10.9$ s, when the high horizontal acceleration $a \approx 0.40g$ was related to the small value $r_u = 0.18$. These high-frequency components can be captured only by adopting advanced soil constitutive models such as Sanisand. Moreover, in order to predict the aforementioned pore-pressure build-up properly, the fully coupled u-p-U formulation would be required to obtain a rigorous solution, because the attainment of liquefaction is contemporary to some pore-pressure dissipation due to the high sand hydraulic conductivity (Zienkiewicz and Shiomi 1984; Taiebat et al. 2010). However, this formulation would be too onerous and time-consuming for the case at hand: therefore, the approximate u-p formulation was adopted, in which the soil skeleton–fluid relative acceleration is disregarded. This assumption may be deemed adequate for fine sands subjected to low-frequency ground motions, as in the case studied in this work (Zienkiewicz et al. 1980).

Fig. 9 plots the contours of the excess pore-water pressure ratio, r_u, obtained under the base excitation BE_16 when full liquefaction

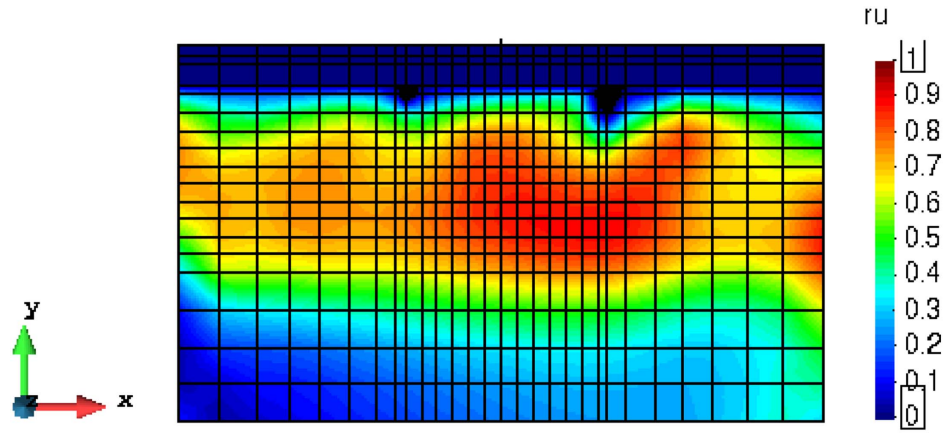

Fig. 9. Contours of the excess pore-water pressure ratio at the time instant at which liquefaction is triggered when subject to base excitation BE_16 ($t = 41.38$ s).

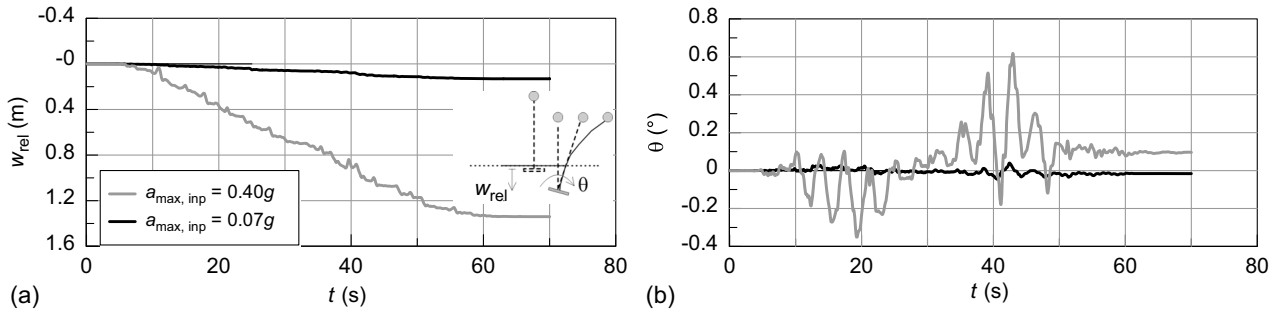

Fig. 10. Time histories obtained with the Imperial Valley base excitations (BE_2 and 16): (a) relative settlement; and (b) raft rotation.

was triggered into the loose sand layer ($t = 41.38$ s). It is apparent that the whole loose sand layer (finer mesh) reached liquefaction r_u(=0.9–1.0), which is spread all over the numerical domain at the depths of the loose sand, whereas lower values of r_u(=0.1–0.5) were attained in the dense sand layer.

The ground motion amplitude also influenced the seismic performance of the OWT (Fig. 10). Specifically, the increase of the seismic input by about 6 times (from 0.07 to 0.40g) caused increases of both the permanent relative settlement and peak rotation of about 10 and 14 times, respectively, thus leading to a potentially unacceptable settlement, equal to 1.34 m, and a high peak rotation, equal to 0.62°. For the permanent tilting, the value $\theta_{perm} = 0.10°$ was computed for the very strong Imperial Valley motion, which is well below the threshold value typically allowed for wind turbines, $\theta_y = 0.50°$ (DNV 2010; Kaynia 2019). This is not surprising because, after the end of the earthquake, the system almost recovered its symmetry along the horizontal direction, because these results were obtained without applying any wind thrust. This remarkable outcome shows the need to combine the operational wind load at the SLS and the seismic loading when assessing the seismic performance of OWTs and the relevant roles, as is discussed in more detail in the next section.

Similar results were obtained with the remaining ground motions adopted in the study, such as the Kobe record and the sinusoidal input (Table 2), which were scaled for the purpose of assessing the influence of the input motion amplitude. The results are given in Fig. 11, which plots the performance indexes against the peak acceleration of the base excitations in terms of permanent values of the dimensionless settlement, $w_{rel,perm}/D$, and rotation, θ_{perm}. In Fig. 11, as in Figs. 14 and 16, distinction between sine waves and real earthquakes is made, the latter term meaning that the relevant base excitations, although being scaled, are not as uniform as sine waves, in terms of both amplitude and frequency content, which vary with time. As expected, increasing settlement and rotation were observed with increasing seismic amplitude: however, there was noticeable scatter for both indices. Moreover, the linear trend in Fig. 11 provides quite low values of the coefficient of determination, R^2. This holds true especially for the permanent tilting, because the system recovered its symmetry following the end of the seismic motion. The results obtained for the sine waves were followed closely by those computed for the real ground motions [BE_1 and BE_2 (Table 2)], except for the two outliers which represent the very strong Imperial Valley motion, which is characterized by a large strong-motion duration, $D_{5\text{-}95} = 40.82$ s. This outcome shows that the observed scattering may be attributed to the inadequacy of $a_{max,inp}$ as the sole IM to be related to the seismic performance of OWTs, together with the strong increase of displacements and rotations observed when liquefaction is triggered, as was the case for $a_{max,inp} = 0.40$ g. Frequency content and strong-motion duration also are expected to influence the response of such systems, as is discussed in the following section.

Frequency Content

The role of frequency content also was investigated by varying the predominant frequency, f_p, of the base excitations. As an example, Fig. 12 shows the moderate sine waves (Table 2) adopted for this purpose, and Fig. 13 plots the time histories of the raft settlement and rotation for the different values assumed for the predominant frequency, namely $f_p = 0.5$, 1.0, and 2.0 Hz. It is apparent that the predominant frequency mainly affects the rate of accrual of the raft

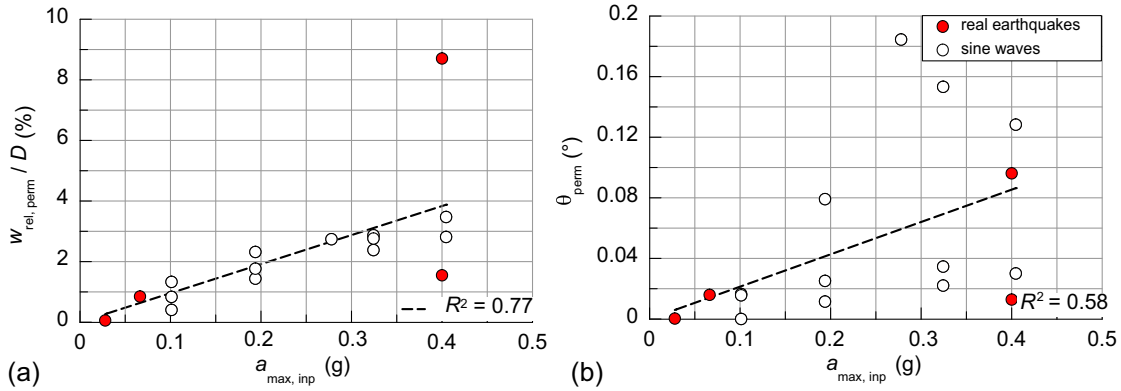

Fig. 11. Permanent values versus peak acceleration of the base excitations: (a) dimensionless relative settlement; and (b) tilting of the raft.

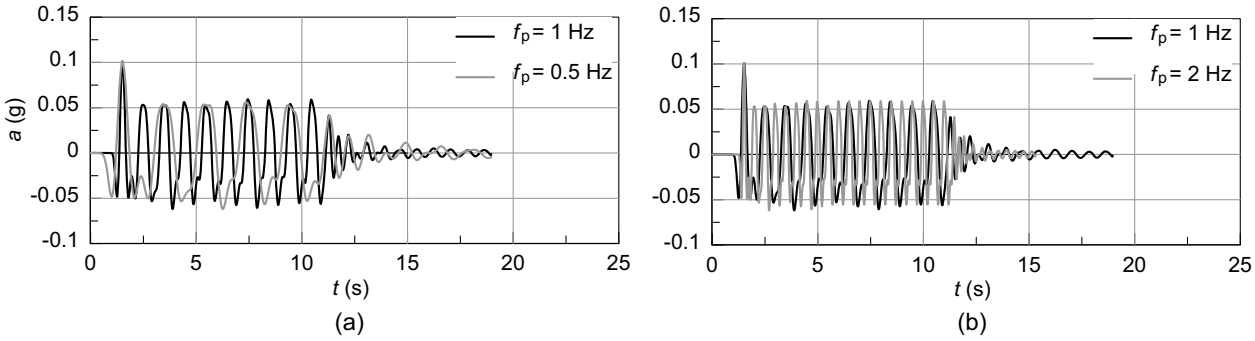

Fig. 12. Time histories of the adopted sine waves (BE_6, 7, and 8) characterized by different predominant frequencies.

settlement [Fig. 13(a)], which decreases with frequency. This may be due to two main concurring mechanisms: first, for a given peak acceleration, the lower the frequency, the higher is the displacement and therefore the higher are the consequent shear strains induced in the soil; and second, the partially drained behavior exhibited by the soil for $f_p = 0.5$ Hz.

Fig. 13 also shows the excess pore-water pressure ratio for the loose sand layer beneath the foundation (Fig. 3, P5) as a function of time [Fig. 13(c)] and the relative settlement, w_{rel} [Fig. 13(d)]. The excess pore-pressure ratio, r_u, computed for a low-frequency input ($f_p = 0.5$ Hz) exhibited much greater fluctuations than those obtained for higher frequencies, reaching almost null values (as much as $r_u = 0.2$), whereas almost no reduction of pore-water pressures occurred for the two remaining frequencies considered herein. Typically, this strong reduction of r_u is not observed when a soil specimen is subjected to fully undrained multistage strain-controlled cyclic triaxial (MSCCTX) tests (Chen et al. 2019); in these tests, an upward shift in the time history of r_u is observed when liquefaction is almost fully triggered ($r_{u\max} \approx 0.9$), so that such low values of r_u are never attained. Therefore the present results may be ascribed to the sandy soil being allowed to partially dissipate excess pore-water pressures between two consecutive cycles when $f_p = 0.5$ Hz, which is not permitted for $f_p = 1.0$ and 2.0 Hz due to the quicker application of the seismic perturbation. This affects the settlement of the system (measured with respect to the far-field one) [Fig. 13(d)]. The reduction of excess pore-water pressures implies an increase of effective stresses, with consequent accumulation of settlement, and also may be attributed to shear-induced dilation. This is confirmed by the greater jumps toward greater settlement of the foundation observed for $f_p = 0.5$ Hz, which follow wider r_u–w_{rel} loops. This should demonstrate the link between the partially drained behavior of the foundation soils and the seismic performance of the OWT, which could have not been captured if fully coupled analyses were not performed.

Regarding the rotation time trace [Fig. 13(b)], the role of f_p is not clear because the minimum permanent tilting is obtained for $f_p = 2.0$ Hz ($\theta_{perm} = 0.01°$), whereas the maximum was computed for $f_p = 1.0$ Hz ($\theta_{perm} = 0.08°$).

Seismic performance indices are presented in Fig. 14 against the predominant frequency f_p. There is a clear, slightly decreasing

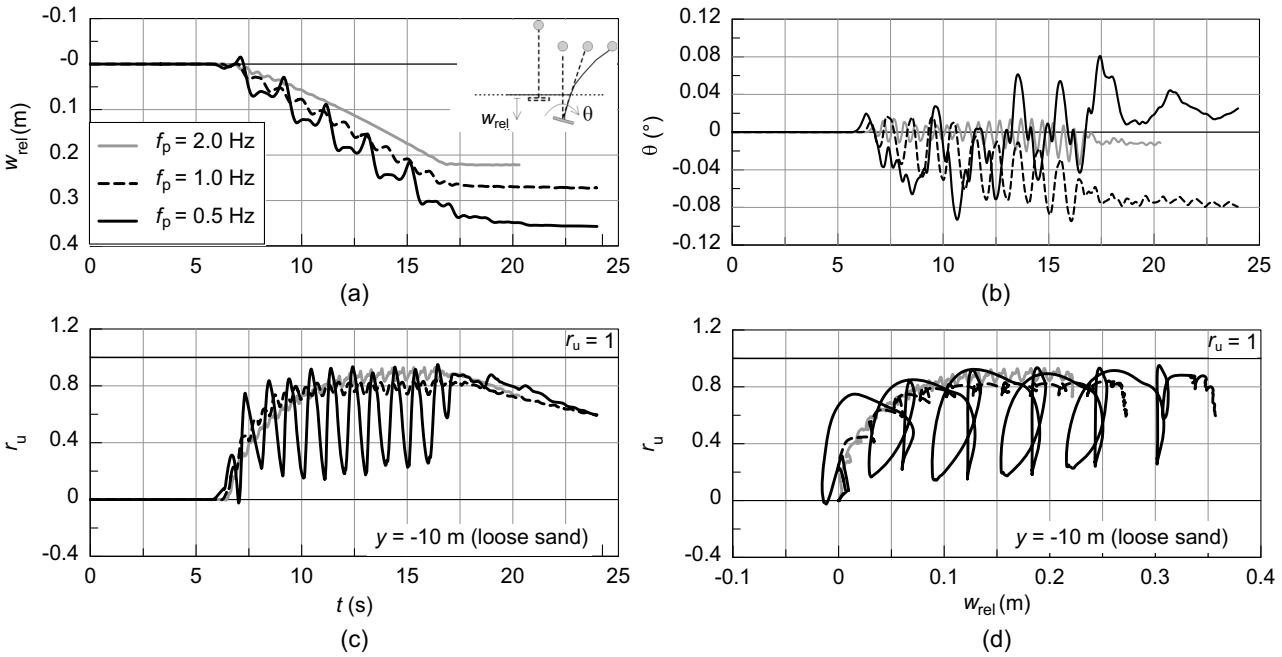

Fig. 13. For moderate sine waves (BE_6, 7, and 8): (a) time histories of relative settlement; (b) time histories of rotation of the raft; (c) excess pore-water pressure ratio recorded beneath the foundation in the loose sand layer (Fig. 3, P5) as a function of time; and (d) excess pore-water pressure ratio recorded beneath the foundation in the loose sand layer (Fig. 3, P5) as a function of relative settlement.

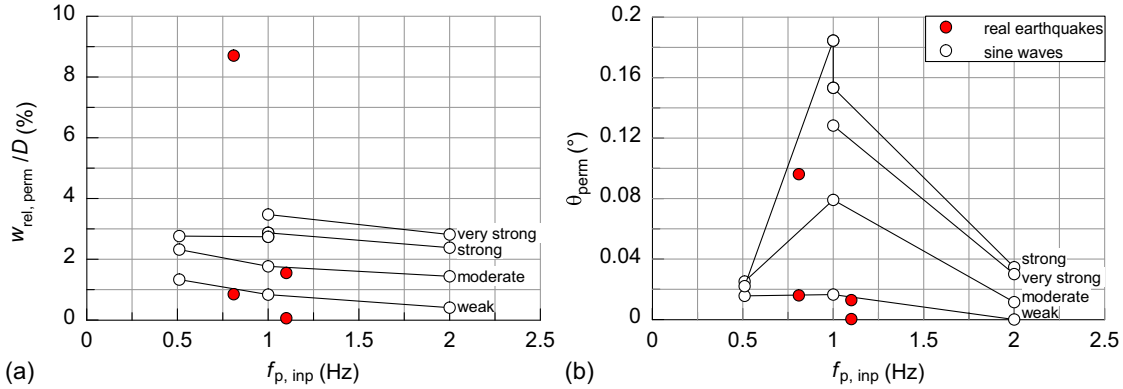

Fig. 14. Permanent values versus the predominant frequency of the base excitations: (a) dimensionless relative settlement; and (b) tilting of the raft.

trend for the settlement, whereas there is a bell-shaped trend for θ_{perm}. The latter may be ascribed to the absence of any wind thrust, which makes the system quasi-symmetric with respect to the horizontal direction, and to the almost-resonance conditions triggered by the seismic input at frequency $f = 1.0$ Hz, which is close to the fundamental frequency of the soil deposit, $f_0 = 1.23$ Hz. This clear trend was not found for the real earthquakes: this key aspect clearly needs further investigation.

Any possible resonance between the base excitations and the system's natural frequency was inhibited due to the huge difference between the fixed-base frequency ($f_s = 0.30$ Hz) and the predominant frequency of the ground motions adopted in the study ($f_p = 0.5$, 0.81, 1.0, 1.1, and 2.0 Hz), as also demonstrated by the Fourier Amplitude spectra in Fig. 4(b). Furthermore, the compliant-base frequency of the system also would be lowered by soil–structure interaction (SSI) effects (Veletsos and Meek 1974), which would contribute to increase this difference. However, higher natural modes of the OWT, e.g., corresponding to the second compliant-base frequency, may be affected by the ground motion frequencies (Panagoulias et al. 2023): further research is required in this respect.

Strong-Motion Duration

The influence of strong-motion duration $D_{5–95}$ on the seismic performance of the system was assessed by comparing the results obtained with the very strong sine wave (BE_15) and the moderate Kobe record (BE_9). These seismic inputs are characterized by the same peak horizontal acceleration ($a_{max,inp} = 0.40g$) and a similar frequency content ($f_p = 1.0$ and 1.1 Hz), but a remarkable difference in terms of $D_{5–95}$, 9.40 and 3.97 s, a ratio of 2.37. The time histories of the foundation settlement relative to the free-field and of the rotation are plotted in Fig. 15 as a function of the dimensionless time t/T_f, where T_f is the total duration of the ground motion, equal to $T_f = 24$ s for BE_15 and to $T_f = 30$ s for BE_9. In Fig. 15, the location of the permanent relative settlement and rotation also is indicated. The comparison clearly shows the noticeable influence of the strong-motion duration on the seismic performance, provided that the inelastic and irreversible soil behavior is triggered; the settlement obtained with the two seismic inputs overlap in the time frame ranging from the beginning ($t/T_f \approx 0.25$) to the end of the strong-motion phase of the input BE_9 ($t/T_f \approx 0.40$). Therefore, it follows that the ratio of the permanent settlements is about 2.2, which is very close to the ratio of the two strong-motion durations. This overlapping of the settlement time traces can be visualized clearly due to the adoption of the dimensionless time, t/T_f, because the accumulation of the permanent relative settlement occurs at different instants in the two base excitations under consideration. The overlapping clearly indicates that the rate of accrual of the relative settlement is almost identical for the two different base excitations, because this depends on the amplitude and frequency content of the seismic input, which implies that the difference in the permanent settlement can be attributed to the different strong-motion durations.

The same concept applies to the peak values of the rigid rotation, the ratio of which is about 2.3, whereas it does not hold for the permanent rotation, because the system is symmetric with respect to the rotation and can recover partially at the end of the dynamic event.

The seismic performance indexes are not plotted against the strong-motion duration, because few values of $D_{5–95}$ were considered in the study (Table 2). It also is apparent that the strong-motion

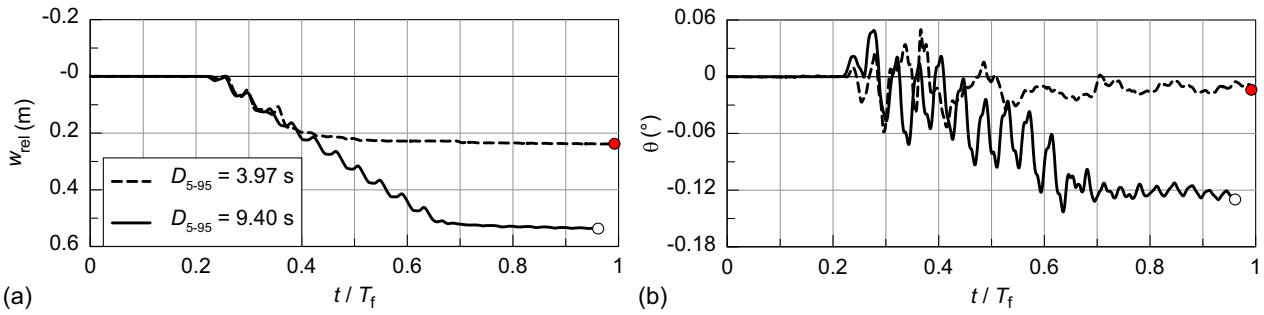

Fig. 15. Time histories for different strong-motion durations (BE_9 and 15): (a) relative settlement; and (b) rigid rotation experienced by the raft foundation.

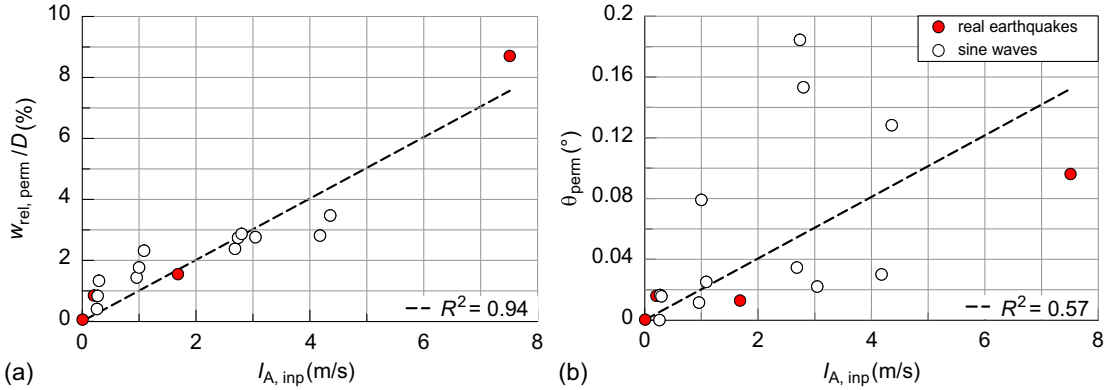

Fig. 16. Permanent values versus Arias intensity of the base excitations: (a) dimensionless relative settlement; and (b) tilting of the raft.

duration alone cannot fully capture the increase in the permanent settlement, because this IM misses both the frequency content and the irregular time distribution of the real ground motions. This is why a cumulative IM is needed, such as the Arias intensity, the influence of which on the seismic performance of OWTs is reported in the following section.

Integral IM: Arias Intensity

The results discussed in the previous sections showed the role of the different seismic input properties, such as amplitude, frequency content, and strong-motion duration, on the seismic performance of OWTs. Because all of them capture a specific aspect of earthquake intensity only, an integral intensity measure, such as the Arias intensity I_A, may be used as a global measure of the energy released by the earthquake (Kramer 1996). This quantity can be related confidently to the permanent settlement and tilting experienced by the raft.

The aforementioned seismic performance indexes are plotted in Fig. 16 against the Arias intensity of all the base excitations adopted in the study, $I_{A,inp}$. The values in this study covered a broad range, from the minimum $I_{A,inp} = 0.01$ m/s (very weak motion) to the maximum $I_{A,inp} = 7.51$ m/s (destructive earthquake), the latter of which is out of the range of real motions.

There was a clear linear tendency for the permanent settlement, as demonstrated by the high value of the coefficient of determination, $R^2 = 0.94$, whereas there was a very disperse trend, characterized by large scattering, for the permanent tilting of the raft ($R^2 = 0.57$). The difference observed between the permanent settlement and the tilting of the system may be attributed again to the asymmetry of the system with respect to the vertical direction along which the body forces act, such as gravity, whereas this does not apply to the horizontal direction, in which the system recovers its symmetry at the end of the seismic event. However, OWTs are likely to be subjected to the operational wind thrust at the time of an earthquake, which will induce asymmetry along the horizontal direction as well, as is discussed in the following section.

Influence of Wind Thrust

The preceding results shed some light on the role of ground motion properties on the seismic performance of OWTs on liquefiable soils. However, this neglected the wind thrust, the role of which in the seismic performance of OWTs is still to be clarified. Therefore, further numerical analyses were carried out to assess the influence of simultaneous application of wind load at the SLS and seismic loading on the seismic performance of the raft foundation.

The influence of wind thrust on the seismic performance was assessed by applying an equivalent static horizontal force at the lumped mass of the tower ($y = 46.4$ m), $F_h = -353.0$ kN, because the static phase precedes the application of the base excitation. This operational wind load provided a moment on the raft foundation equal to 16,944 kN · m, which represents the wind loads in the field conditions. The negative value means that the force acted opposite to the x-axis reported in Fig. 5: this was done to make the static force concordant with the dynamic force induced by the first peak of the base excitations, and hence to maximize the destabilizing effect of the wind loading, as typically is done in current practice. This entails a bias on the rotation of the raft foundation, similar to the effect of gravity on the raft settlement. In the analyses, geometrical second-order (P-δ) effects were considered, although these effects may be minor. The main purpose of this section is to study the effect of the wind loading on the seismic performance of OWTs, which justifies the simplified representation of the wind thrust as a static equivalent horizontal load, thus neglecting its cyclic nature.

The results of the analyses carried out with and without the wind thrust are presented in Figs. 17 and 18 for the base excitations BE_2 (weak) and BE_15 (very strong), respectively, in terms of time histories of relative settlement and rigid rotation of the raft foundation. The settlement of the foundation was almost insensitive to the horizontal load induced by the wind, because the vertical and horizontal directions basically are uncoupled, whereas the rotation is influenced strongly by the wind thrust. For the Imperial Valley ground motion (Fig. 17), a clear bias was introduced along the horizontal direction, and the permanent tilting of the system was −0.28°, whereas it was about −0.01° in the absence of the wind thrust, a remarkable increase of about 30 times. Therefore, a huge increment was observed. However, the seismic performance of the raft still was satisfactory, because the permanent rotation θ_{perm} still was below the threshold of 0.50°, due to the low intensity of the ground motion applied ($a_{max,inp} = 0.07g$).

Similar results were obtained by applying the very strong sine wave ground motion [BE_15 (Fig. 18)]. Again, the rotation was negative, and attained a maximum value, this time equal to the permanent value, of about −1.30°, much higher than the value of −0.13° experienced by the raft foundation without the wind thrust, an increase of about 10 times. In this extreme case, permanent tilting was far beyond the threshold permanent tilting, $\theta_y = 0.50°$, due to the very strong ground motion considered. It may be concluded that the system is asymmetric not only regarding the vertical

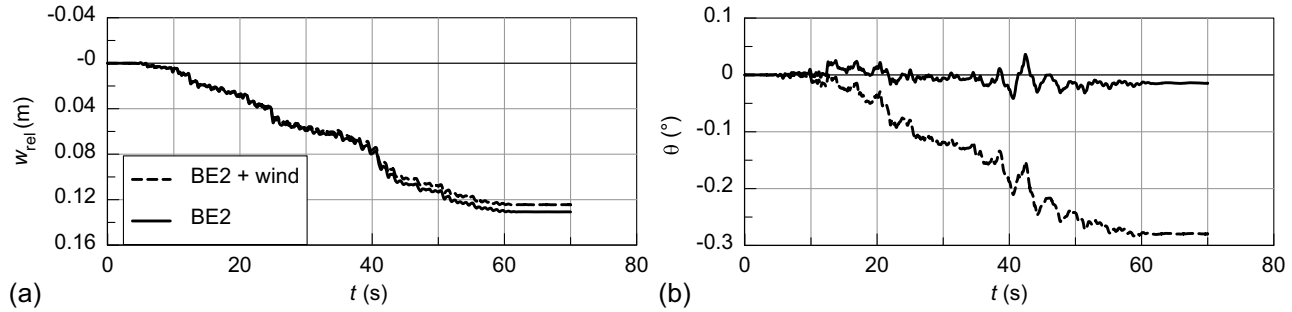

Fig. 17. Influence of wind thrust when applying the weak Imperial Valley base excitation (BE_2) on the time histories of (a) relative settlement; and (b) rigid rotation of the raft foundation.

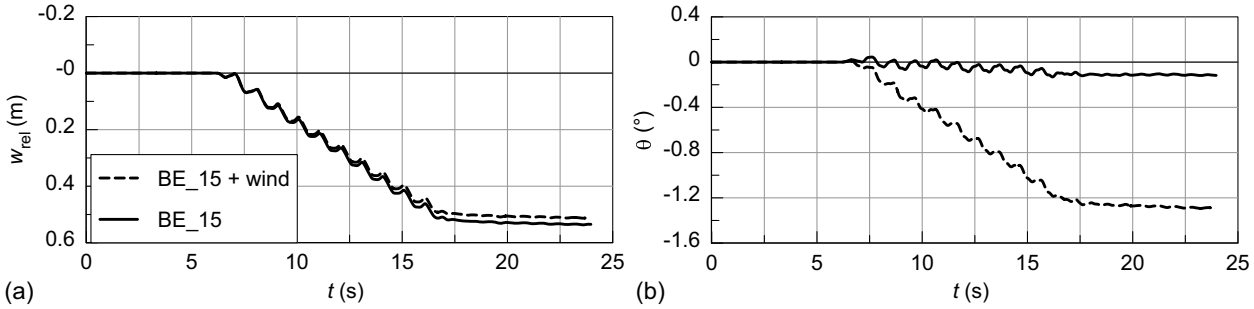

Fig. 18. Influence of wind thrust when applying a very strong sine wave (BE_15) on the time histories of (a) relative settlement; and (b) rigid rotation of the raft foundation.

direction (settlement always in the same direction of gravity, of course), but along the rotational direction as well, due to the presence of the operational wind load.

Design Implications

The preceding numerical FE model (i.e., the small FE model) proved to be effective in reproducing the experimental results obtained in the centrifuge, and therefore was used to quantify the relative influence of ground motions and wind thrust.

This entailed the following useful design implications:

1. Centrifuge tests using the ESB container may be adopted to assess the seismic performance of OWTs on liquefiable soils. However, the deviance of the experimental results from the seismic performance in the field may differ by about 30% for the raft and by about 20% for the tower, as was confirmed by the preceding results (Figs. 6 and 7) and by Gaudio et al. (2023).
2. Therefore, a small FE model may be implemented to extend the centrifuge testing campaign, which typically is too onerous to perform. Numerical parametric studies may be successfully carried out, provided that an advanced soil constitutive model and the *u-p* formulation (at least) are adopted; otherwise, the influence of ground motion properties will not be captured properly. This would allow the development of more-reliable empirical relations for a preliminary assessment of the seismic performance of OWTs on liquefiable soils, as a function of some selected intensity measures of the ground motion.
3. The effect of simultaneous application of the operational wind load and seismic loading is more crucial for the residual tilting than for the settlement of the raft foundation. Specifically, the presence of the wind thrust may increase the permanent tilting of the structure strongly, as much as about 30 times, when the structure is hit by a strong earthquake capable of triggering soil liquefaction. This wind thrust may bring the rotation beyond the threshold value indeed, which typically constitutes the tightest design requirement of such structures.

Summary and Conclusions

In this paper, a numerical model was implemented in the finite-element OpenSees framework to assess the role of ground motion IMs and the relative influence of the operational wind thrust on the seismic performance of OWTs on liquefiable soils. This field scenario has emerged as a frequent case in seismic-prone areas, such as the Californian coastline and East Asia, where the need for alternative energy sources to fossil fuels has been shaping the environment.

A 3D FE model was calibrated against dynamic centrifuge tests carried out at the Schofield Centre, University of Cambridge, UK, in the relatively small equivalent shear beam model container. A small numerical model representing the ESB size was implemented in OpenSees; here, a set of both hydraulic and mechanical Sanisand constitutive parameters, which were calibrated in previous works against centrifuge tests, were adopted. A numerical parametric study, extending the experimental study, was carried out to study the influence of the amplitude, frequency content, strong-motion duration, and Arias intensity of the seismic input. The outcomes showed that the influence of amplitude typically is strongly nonlinear, because an increase in $a_{max,inp}$ by about 7 times produced a higher growth in the peak settlements and tilting of the system, depending on the remaining properties of the motion.

The frequency content mostly influences the accumulation rate of both settlement and rotation of the raft, which decreased with

increasing frequency. This key result of the paper was shown to depend on both the partially drained response of the liquefiable sandy soils and the increasing shear demand imposed by increasing frequencies on the soil deposit.

Finally, the strong-motion duration influences the time frame in which permanent settlements and tilting are accumulated, provided that soil liquefaction is triggered. However, this intensity measure does not take frequency content into account, and therefore misses some key feature of ground motions, which affects the seismic performance of OWTs. In this framework, Arias intensity proved to be the best parameter to adopt to predict the permanent settlement of the raft, because it is a cumulative, integral intensity measure, encompassing the amplitude, the frequency content, and the strong-motion duration of the input motion.

All the aforementioned results were obtained without applying any wind thrust, whereas applying a typical value for the operational load the wind thrust increased the OWT permanent tilting by as much as 30 times for the specific case under consideration. Therefore this wind brought the rotation beyond the threshold value indeed ($\theta_y = 0.50°$), due to the nonsymmetric conditions imposed by the relevant horizontal loading. This latter crucial point also involves the nonsymmetric soil stress state induced beneath the raft foundation, which is caused by the nonlinear and irreversible soil behavior.

Cleary, a larger number of real ground motions would be useful to provide a more comprehensive analysis and further confirm or extend the results obtained in this paper. Moreover, the influence of wind thrust should be studied considering its cyclic nature.

The novel results obtained in this study may contribute favorably to the overall body of knowledge for the design of OWTs in seismic-prone areas.

Data Availability Statement

Some or all data, models, or code that support the findings of this study are available from the corresponding author upon reasonable request.

Acknowledgments

The centrifuge experiment was performed with the excellent help of technicians at the Schofield Centre of Cambridge University. This support is acknowledged.

References

Adamidis, O., and S. P. G. Madabhushi. 2015. "Use of viscous pore fluids in dynamic centrifuge modelling." *Int. J. Phys. Modell. Geotech.* 15 (3): 141–149. https://doi.org/10.1680/jphmg.14.00022.

Adamidis, O., and S. P. G. Madabhushi. 2022. "Rocking response of structures with shallow foundations on thin liquefiable layers." *Géotechnique* 72 (2): 127–145. https://doi.org/10.1680/jgeot.19.P.077.

Arias, A. 1970. "A measure of earthquake intensity." In *Seismic design for nuclear power plants*, edited by R. Hansen, 438–483. Cambridge, MA: MIT Press.

Chen, G., D. Zhao, W. Chen, and C. H. Juang. 2019. "Excess pore-water pressure generation in cyclic undrained testing." *J. Geotech. Geoenviron. Eng.* 145 (7): 04019022. https://doi.org/10.1061/(ASCE)GT.1943-5606.0002057.

Dafalias, Y. F., and M. T. Manzari. 2004. "Simple plasticity sand model accounting for fabric change effects." *J. Eng. Mech.* 130 (6): 622–634. https://doi.org/10.1061/(ASCE)0733-9399(2004)130:6(622).

Desmond, C., J. Murphy, L. Blonk, and W. Haans. 2016. "Description of an 8 MW reference wind turbine." *J. Phys.: Conf. Ser.* 753 (9): 092013. https://doi.org/10.1088/1742-6596/753/9/092013.

DNV (Det Norske Veritas). 2010. *Design of offshore wind turbine structures*. DNV-OS-J101. Høvik, Norway: DNV.

DNV (Det Norske Veritas). 2018. *Support structures for wind turbines*. DNVGL-ST-0126. Høvik, Norway: DNV.

DNV (Det Norske Veritas). 2021. *Seismic design of wind power plants*. DNV-RP-0585. Høvik, Norway: DNV.

Gaudio, D., and S. Rampello. 2016. "Dynamic soil-structure interaction of bridge-pier caisson foundations." *Procedia Eng.* 158 (Jan): 146–151. https://doi.org/10.1016/j.proeng.2016.08.420.

Gaudio, D., J. Seong, S. K. Haigh, G. M. B. Viggiani, S. P. G. Madabhushi, R. Shrivatsava, R. Veluvolu, and P. Padhy. 2023. "Boundary effects on dynamic centrifuge modelling of onshore wind turbines on liquefiable soils." *Int. J. Phys. Modell. Geotech.* 23 (1): 16–34. https://doi.org/10.1680/jphmg.21.00085.

Idriss, I. M., and H. B. Seed. 1968. "Seismic response of horizontal soil layers." *J. Soil Mech. Found. Div.* 94 (4): 1003–1031. https://doi.org/10.1061/JSFEAQ.0001163.

Kaynia, A. M. 2019. "Seismic considerations in design of offshore wind turbines." *Soil Dyn. Earthquake Eng.* 124 (Sep): 399–407. https://doi.org/10.1016/j.soildyn.2018.04.038.

Kementzetzidis, E., S. Corciulo, W. G. Versteijen, and F. Pisanò. 2019. "Geotechnical aspects of offshore wind turbine dynamics from 3D nonlinear soil-structure simulations." *Soil Dyn. Earthquake Eng.* 120 (May): 181–199. https://doi.org/10.1016/j.soildyn.2019.01.037.

Kramer, S. L. 1996. *Geotechnical earthquake engineering*. London: Pearson.

Kuhlemeyer, R. L., and J. Lysmer. 1973. "Finite element method accuracy for wave propagation problems." *J. Soil Mech. Found. Div.* 99 (5): 421–427. https://doi.org/10.1061/JSFEAQ.0001885.

Madabhushi, S. P. G., S. K. Haigh, N. E. Houghton, and E. Gould. 2012. "Development of a servo-hydraulic earthquake actuator for the Cambridge Turner beam centrifuge." *Int. J. Phys. Modell. Geotech.* 12 (2): 77–88. https://doi.org/10.1680/ijpmg.11.00013.

Madabhushi, S. P. G., N. E. Houghton, and S. K. Haigh. 2006. "A new automatic sand pourer for model preparation at University of Cambridge." In *Proc., 6th Int. Conf. on Physical Modelling in Geotechnics*, edited by C. W. W. Ng, L. M. Zhang, and Y. H. Wang, 217–222. London: Taylor and Francis.

Madabhushi, S. P. G., D. Patel, and S. K. Haigh. 2005. *Geotechnical aspects of the Bhuj earthquake*. Chapter 3, EEFIT Rep. London: Institution of Structural Engineers.

Newmark, N. M. 1959. "A method of computation for structural dynamics." *J. Eng. Mech. Div.* 85 (3): 67–94. https://doi.org/10.1061/JMCEA3.0000098.

Panagoulias, S., C. de Winter, S. T. Navalkar, and A. Nernheim. 2023. "Sensitivity of the seismic response of monopile-supported offshore wind turbines to soil variability." *Ocean Eng.* 268 (Jan): 113545. https://doi.org/10.1016/j.oceaneng.2022.113545.

Ramirez, J., A. R. Barrero, L. Chen, S. Dashti, A. Ghofrani, M. Taiebat, and P. Arduino. 2018. "Site response in a layered liquefiable deposit: Evaluation of different numerical tools and methodologies with centrifuge experimental results." *J. Geotech. Geoenviron. Eng.* 144 (10): 04018073. https://doi.org/10.1061/(ASCE)GT.1943-5606.0001947.

Salvatore, E., R. Proia, G. Modoni, E. Andò, and G. Viggiani. 2017. "Influenza delle condizioni sperimentali delle prove triassiali su sabbie." [In Italian.] In *Proc., Incontro Annuale dei Ricercatori di Geotecnica 2017*, 1–6. Potenza, Italy: Editrice Universosud.

Scott, M. H., and G. L. Fenves. 2010. "Krylov subspace accelerated Newton algorithm: Application to dynamic progressive collapse simulation of frames." *J. Struct. Eng.* 136 (5): 473–480. https://doi.org/10.1061/(ASCE)ST.1943-541X.0000143.

Seong, J., S. K. Haigh, S. P. G. Madabhushi, R. Shrivastava, R. Veluvolu, and P. Padhy. 2022. "On seismic protection of wind turbine foundations founded on liquefiable soils." *Soil Dyn. Earthquake Eng.* 159 (Aug): 107327. https://doi.org/10.1016/j.soildyn.2022.107327.

Taiebat, M., B. Jeremić, Y. F. Dafalias, A. M. Kaynia, and Z. Cheng. 2010. "Propagation of seismic waves through liquefied soils." *Soil Dyn.*

Earthquake Eng. 30 (4): 236–257. https://doi.org/10.1016/j.soildyn.2009.11.003.

Tarque Ruiz, S. N. 2020. "Programa compilado OpenSees, mayo 2020. Peru." Accessed March 28, 2023. https://www.researchgate.net/publication/377415389_Compiled_code_for_OpenSees?channel=doi&linkId=65a9210fa59bf45fc9d52ad6&showFulltext=true.

Trifunac, M. D., and A. G. Brady. 1975. "A study on the duration of strong earthquake ground motion." *Bull. Seismol. Soc. Am.* 65 (3): 581–626. https://doi.org/10.1785/BSSA0650030581.

Vacareanu, V., E. Kementzetzidis, and F. Pisano. 2019. "3D FE seismic analysis of a monopile-supported offshore wind turbine in a non-liquefiable soil deposit." In *Proc., 2nd Int. Conf. on Natural Hazards and Infrastructure (ICONHIC2019)*, edited by G. Gazetas and I. Anastasopoulos, 1–11. Athens, Greece: National Technical Univ. of Athens.

Veletsos, A. S., and J. W. Meek. 1974. "Dynamic behaviour of building-foundation systems." *Earthquake Eng. Struct. Dyn.* 3 (2): 121–138. https://doi.org/10.1002/eqe.4290030203.

Yang, Z., J. Lu, and A. Elgamal. 2008. *OpenSees soil models and solid-fluid fully coupled elements: User's manual*. San Diego: Dept. of Structural Engineering, Univ. of California.

Zienkiewicz, O. C., C. T. Chang, and P. Bettess. 1980. "Drained, undrained, consolidating and dynamic behaviour assumptions in soils." *Géotechnique* 30 (4): 385–395. https://doi.org/10.1680/geot.1980.30.4.385.

Zienkiewicz, O. C., and T. Shiomi. 1984. "Dynamic behaviour of saturated porous media; the generalized Biot formulation and its numerical solution." *Int. J. Numer. Anal. Methods Geomech.* 8 (1): 71–96. https://doi.org/10.1002/nag.1610080106.